Bulk Scattering Properties for the Remote Sensing of Ice Clouds. Part II: Narrowband Models

BRYAN A. BAUM,* PING YANG,+ ANDREW J. HEYMSFIELD,# STEVEN PLATNICK,@ MICHAEL D. KING,@ Y.-X. HU,* AND SARAH T. BEDKA&

*NASA Langley Research Center, Hampton, Virginia
+Texas A&M University, College Station, Texas
#National Center for Atmospheric Research,** Boulder, Colorado
@NASA Goddard Space Flight Center, Greenbelt, Maryland
&Cooperative Institute for Meteorological Satellite Studies, Madison, Wisconsin

ABSTRACT

This study examines the development of bulk single-scattering properties of ice clouds, including single-scattering albedo, asymmetry factor, and phase function, for a set of 1117 particle size distributions obtained from analysis of the First International Satellite Cloud Climatology Project Regional Experiment (FIRE)-I, FIRE-II, Atmospheric Radiation Measurement Program intensive observation period, Tropical Rainfall Measuring Mission Kwajalein Experiment (KWAJEX), and the Cirrus Regional Study of Tropical Anvils and Cirrus Layers (CRYSTAL) Florida Area Cirrus Experiment (FACE) data. The primary focus is to develop band-averaged models appropriate for use by the Moderate Resolution Imaging Spectroradiometer (MODIS) imager on the Earth Observing System *Terra* and *Aqua* platforms, specifically for bands located at wavelengths of 0.65, 1.64, 2.13, and 3.75 μm. The results indicate that there are substantial differences in the bulk scattering properties of ice clouds formed in areas of deep convection and those that exist in areas of much lower updraft velocities. Band-averaged bulk scattering property results obtained from a particle-size-dependent mixture of ice crystal habits are compared with those obtained assuming only solid hexagonal columns. The single-scattering albedo is lower for hexagonal columns than for a habit mixture for the 1.64-, 2.13-, and 3.75-μm bands, with the differences increasing with wavelength. In contrast, the asymmetry factors obtained from the habit mixture and only the solid hexagonal column are most different at 0.65 μm, with the differences decreasing as wavelength increases. At 3.75 μm, the asymmetry factor results from the two habit assumptions are almost indistinguishable. The asymmetry factor, single-scattering albedo, and scattering phase functions are also compared with the MODIS version-1 (V1) models. Differences between the current and V1 models can be traced to the microphysical models and specifically to the number of both the smallest and the largest particles assumed in the size distributions.

---

1. Introduction

The general approach for inferring ice cloud optical and microphysical properties from satellite imagery is to compare measured satellite radiances with radiative transfer (RT) calculations. The RT calculations account for viewing geometry, solar illumination, surface temperature, surface emissivity, surface albedo, and bidirectional reflectance characteristics in addition to cloud macrophysical, microphysical, and optical properties (King et al. 1992; Platnick et al. 2003). In this study, our goal is to demonstrate how ice cloud in situ measurements can be used to improve the range of bulk microphysical and optical properties in RT models. The focus in Baum et al. (2005, hereinafter Part I) of this study is on the cloud microphysical models, including the ice particle size and habit distributions. In this paper, the objective is to use the microphysical models to derive bulk optical properties. As a demonstration of the approach, bulk scattering properties are derived for four visible and near-infrared bands on the Moderate Resolution Imaging Spectroradiometer (MODIS).

The current operational MODIS cloud microphysical and optical retrievals are based on a set of 12 cirrus particle size distributions (Baum et al. 2000; King et al. 2004) and are referred to henceforth as version 1, or V1. The cirrostratus and cirrus uncinus distributions are described by Heymsfield (1975), and Heymsfield and Platt (1984) present two modified size distributions typical of warm and cold cirrus clouds and three additional size distributions derived from observations of midlatitude cirrus at temperature $T = -20°C$, $T = -40°C$, and $T = -60°C$. The remaining three models are from specific dates during the First International Satellite Cloud Climatology Project Regional Experiment (FIRE)-I field campaign. In the MODIS V1 models, the ice water content (IWC) ranges from 10^{-3} to 10^{-1} g m^{-3}. The 12 size distributions cover a limited range of cloud microphysical properties and dynamical regimes, for example, production in slowly ascending parcels with updraft speeds of less than 100 cm s^{-1}. Whereas the ice particle size distributions vary among the V1 models, the scattering-property calculations are limited to five discrete particle size bins. When the maximum dimension D is small ($D < 70 \mu$m), that is, for small ice crystals, the habits are prescribed as 50% bullet rosettes, 25% hexagonal plates, and 25% hollow columns. When $D > 70 \mu$m, the habit mixture is 30% aggregates, 30% bullet rosettes, 20% hexagonal plates, and 20% hollow columns. This mixture of habits is fixed for all 12 distributions in the V1 models.

In this study, our intent is to form a new set of ice cloud models based upon an extended set of particle size distributions (PSD) developed from in situ measurements that are more recent than those used in the development of the MODIS V1 models. The new ice cloud models represent a significant improvement in the treatment of both the size distribution and the use of particle habits. The new models are based on 45 size bins, and the mixture of particle habits for each model is based on the analyses of Part I.

Section 2 presents the scattering property libraries used in our analyses, and section 3 outlines the development of the new models. Bulk scattering properties are provided in section 4, and section 5 summarizes and concludes our study.

2. Data and models

a. Moderate Resolution Imaging Spectroradiometer

MODIS is a 36-channel whiskbroom scanning radiometer. The channels, known as bands in the MODIS terminology, span a range from 0.415 to 14.23 μm in four focal plane assemblies (Barnes et al. 1998). Nadir spatial resolutions are 250 m (two bands at 0.65 and 0.86 μm), 500 m (five bands at 0.47, 0.56, 1.24, 1.64, and 2.13 μm), and 1000 m (29 bands). Each band's spectral response function is determined by an interference filter overlying a detector array that images a 10-km along-track swath for each scan, resulting in 40, 20, and 10 element arrays for the 250-, 500-, and 1000-m bands, respectively. MODIS has onboard calibration consisting of blackbodies for the IR bands, a solar diffuser panel for reflectance calibration up through the 2.1-μm MODIS band, and an accompanying solar diffuser stability monitor for assessing the stability of the diffuser up to 1 μm. Two MODIS instruments are currently in orbit on the Earth Observing System (EOS) platforms, each at an altitude of 705 km. The *Terra* platform is in a descending orbit with an equatorial crossing of 1030 local time, and *Aqua* is in an ascending orbit with an equatorial crossing of 1330 local time.

Although no MODIS data are analyzed in this study, bulk scattering models are developed based on the spectral response functions for four MODIS bands: band 1 (0.61–0.68 μm), band 6 (1.60–1.66 μm), band 7 (2.06–2.17 μm), and band 20 (3.65–3.95 μm). For calculations involving the ice-particle scattering-property database described in the following section, bands 1, 6, and 7 are divided into subbands at 0.01-μm resolution, and band 20 is divided into subbands at 0.05-μm resolution.

b. Ice-particle scattering properties

An extensive library of scattering properties has been developed for a set of ice particles that includes droxtals, hexagonal plates, hollow columns, solid columns, three-dimensional bullet rosettes, and aggregates. The methods generally involve a combination of the improved geometric optics approach and the finite-difference time domain method (Yang and Liou 1996a,b). The geometric details for various ice-particle habits can be found in Yang and Liou (1998). Droxtals are described further in Yang et al. (2003) and Zhang et al. (2004).

The droxtal is used to represent the smallest particles in a size distribution and has an aspect ratio approaching unity. Polycrystals include three-dimensional bullet rosettes and aggregates. Aggregates are composed of between two and eight hexagonal columns that are attached together in a random fashion. The scattering-property database has been derived at 234 discrete wavelengths between 0.4 and 13 μm. Scattering properties have been computed for particles in 45 size bins

spanning a maximum dimension range D_{max} from 2 μm to 9.5 mm. For droxtals, scattering properties have been calculated only for sizes up to 200 μm.

The ice-particle databases include properties such as volume V, projected area A, asymmetry factor g, scattering cross section σ_{sca}, extinction cross section σ_{ext}, single-scattering albedo $\tilde{\omega}$, the scattering phase function $P(\Theta)$ (where Θ is the scattering angle), and δ-function transmission. All properties are averaged over a random orientation of the particle. As discussed by Takano and Liou (1989), a large energy component called the δ-function transmission (or simply δ transmission) is produced when rays undergo two refractions at $\Theta = 0°$ through parallel planes in an ice particle. The δ transmission can be significant for pristine ice crystals such as bullet rosettes, hexagonal plates, and hexagonal columns at visible and near-infrared wavelengths. The ratio of the δ transmission energy (at $\Theta = 0°$) to the total scattered energy (all Θ) is denoted by f_δ.

Values of f_δ are shown in Fig. 1 for four habits (3D bullet rosettes, hollow and solid columns, and plates) at three specific wavelengths: 0.65, 1.64, and 2.13 μm. The contribution of δ transmission at 3.75 μm is negligible because of ice absorption and is not provided in the figure. The value of f_δ is near zero for small particle sizes. Droxtals are not included in the figure because such particles are used only for $D_{max} < 60$ μm and f_δ has values near zero for these small sizes. Also, aggregates are not included because the particle is roughened and f_δ is negligible over the entire size range. At a nonabsorbing wavelength (0.65 μm), the f_δ values tend to increase with increasing particle size. For absorbing wavelengths (1.64 and 2.13 μm), the value of f_δ decreases as D_{max} increases because of increasing absorption within the particle.

Figure 2 shows the asymmetry factor at wavelengths of 0.65, 1.64, 2.13, and 3.75 μm, and the ice aggregate is included in addition to the habits shown in the previous figure. The values of g are very sensitive to particle habit in general, with values increasing as D_{max} increases from 2 to 1000 μm. These results are expected as light scattering becomes more isotropic for small particles, which decreases g. In general, particles with $D_{max} > 2000$ μm have larger values of g than the smaller particles. Plates tend to have the highest values of g overall at the visible and weakly absorbing wavelengths. Note that the asymmetry factor in our scattering library includes the contribution of the δ transmission. The influence of δ transmission on the asymmetry factor is provided in the following relationship:

$$g^* = \frac{g - f_\delta}{1 - f_\delta}, \tag{1}$$

where g is the value in our scattering library and g^* represents the asymmetry factor without incorporation of f_δ. The effect of δ transmission is to increase the value of the asymmetry factor.

The single-scattering albedo is shown in Fig. 3 at 1.64, 2.13, and 3.75 μm. In general, $\tilde{\omega}$ decreases with increasing D_{max}, with values being sensitive to habit. Except for the smallest particles, plates tend to have the highest values of $\tilde{\omega}$ while aggregates have the lowest values. Note that $\tilde{\omega}$ also includes the contribution of the δ transmission through the relationship

$$\tilde{\omega}^* = \frac{(1 - f_\delta)\tilde{\omega}}{1 - f_\delta\tilde{\omega}}, \tag{2}$$

where $\tilde{\omega}^*$ represents the single-scattering albedo that does not incorporate the value of f_δ. The effect of δ transmission is to increase the value of $\tilde{\omega}$.

While the library values of g and $\tilde{\omega}$ include the contribution of the δ transmission, $P(\Theta)$ has been azimuthally averaged, scaled by a factor of $(1 - f_\delta)$, and subsequently normalized such that $(1/2)\int_0^\pi P(\Theta) \sin\Theta \, d\Theta = 1$.

3. Band-averaged bulk scattering properties

Table 1 lists the MODIS bands used in this study. The MODIS V1 models were built from ice crystal scattering calculations obtained at a central wavelength for each band. As in Nasiri et al. (2002), scattering calculations in this study are performed at discrete wavelengths and then averaged over the spectral response function for each band. For MODIS solar bands ($\lambda < 3$ μm), the scattering properties at each wavelength within the band's response function are weighted additionally by the solar spectral irradiance $S(\lambda)$ (Kurucz et al. 1984; Neckel and Labs 1984). For wavelengths longer than 3 μm, however, the solar spectrum $S(\lambda)$ is replaced with the Planck function $B(\lambda)$ to represent the thermal IR emission from an opaque ice cloud at 233 K.

The band-weighted mean scattering cross section is given by

$$\overline{\sigma}_{sca} = \frac{\int_{\lambda_1}^{\lambda_2} \int_{D_{min}}^{D_{max}} \left[\sum_{h=1}^{M} \sigma_{sca,h}(D, \lambda)f_h(D) \right] \times n(D)F_s(\lambda)S(\lambda) \, dD \, d\lambda}{\int_{\lambda_1}^{\lambda_2} \int_{D_{min}}^{D_{max}} \left[\sum_{h=1}^{M} f_h(D) \right] n(D)F_s(\lambda)S(\lambda) \, dD \, d\lambda}, \tag{3}$$

a) 0.65 μm

b) 1.64 μm

c) 2.13 μm

-·-·-·-· **3D Bullet Rosette**
············· **Hollow Column**
− − − − − **Solid Column**
——— **Plate**
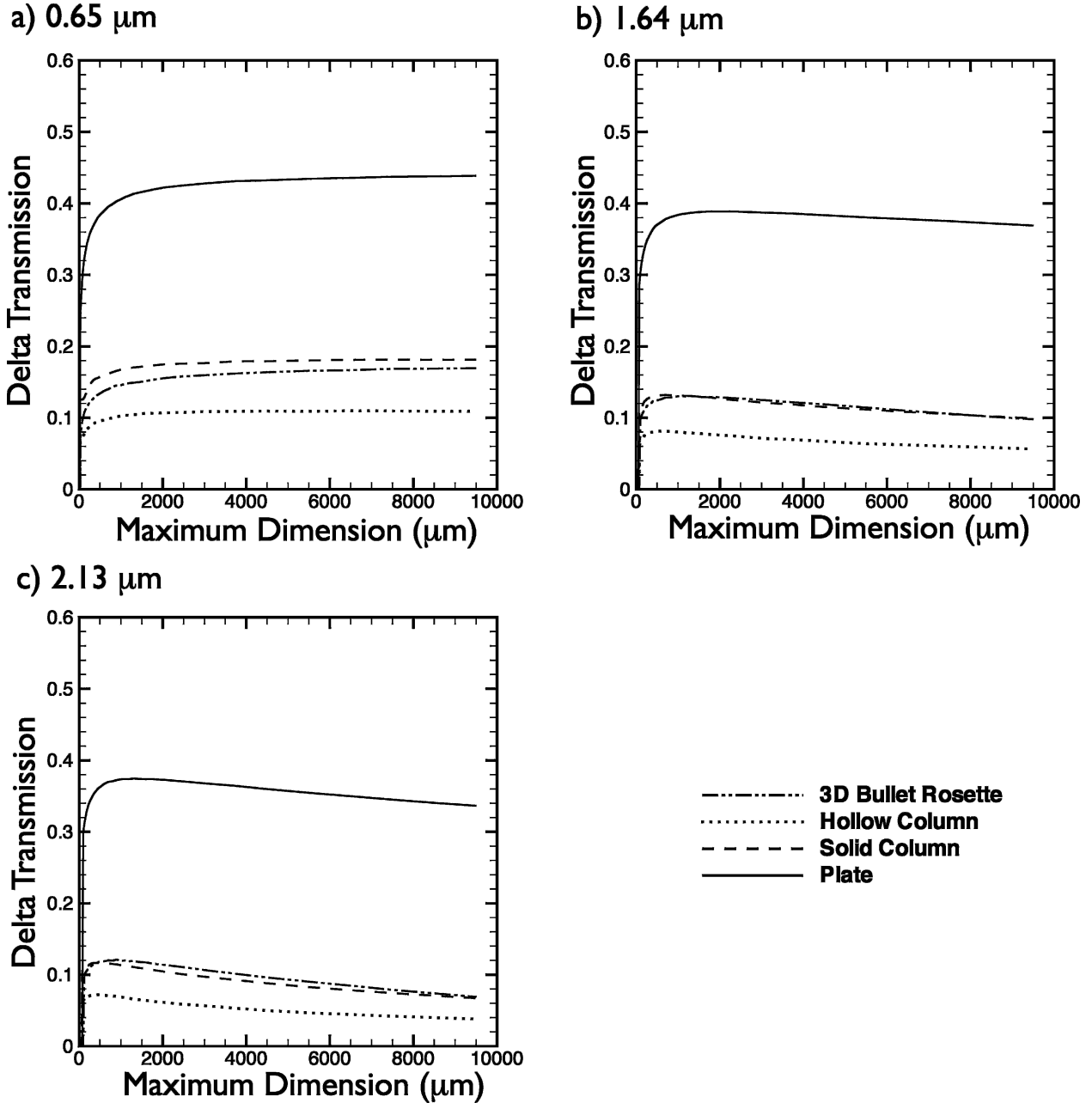
FIG. 1. Fraction of δ transmission energy f_δ as a function of particle maximum dimension D_{max} for four ice particle habits (3D bullet rosette, hollow column, solid column, and hexagonal plate) at (a) 0.65, (b) 1.64, and (c) 2.13 μm. Aggregates are not shown because the value of f_δ is essentially zero because the particle is roughened. Droxtals are not shown because they are implemented only for the smallest particles in each PSD, and f_δ is negligible for very small particles.

where $f_h(D)$ is the ice particle habit fraction for habit h, M is the number of habits, D is particle size, $n(D)$ is the particle density, λ is wavelength, $S(\lambda)$ is the spectral solar spectrum, and $F_s(\lambda)$ is the spectral response function. The habit fraction is defined so that, for each size bin,

$$\sum_{h=1}^{M} f_h(D) = 1. \qquad (4)$$

The band-weighted mean extinction cross section is given by

a) 0.65 μm

b) 1.64 μm
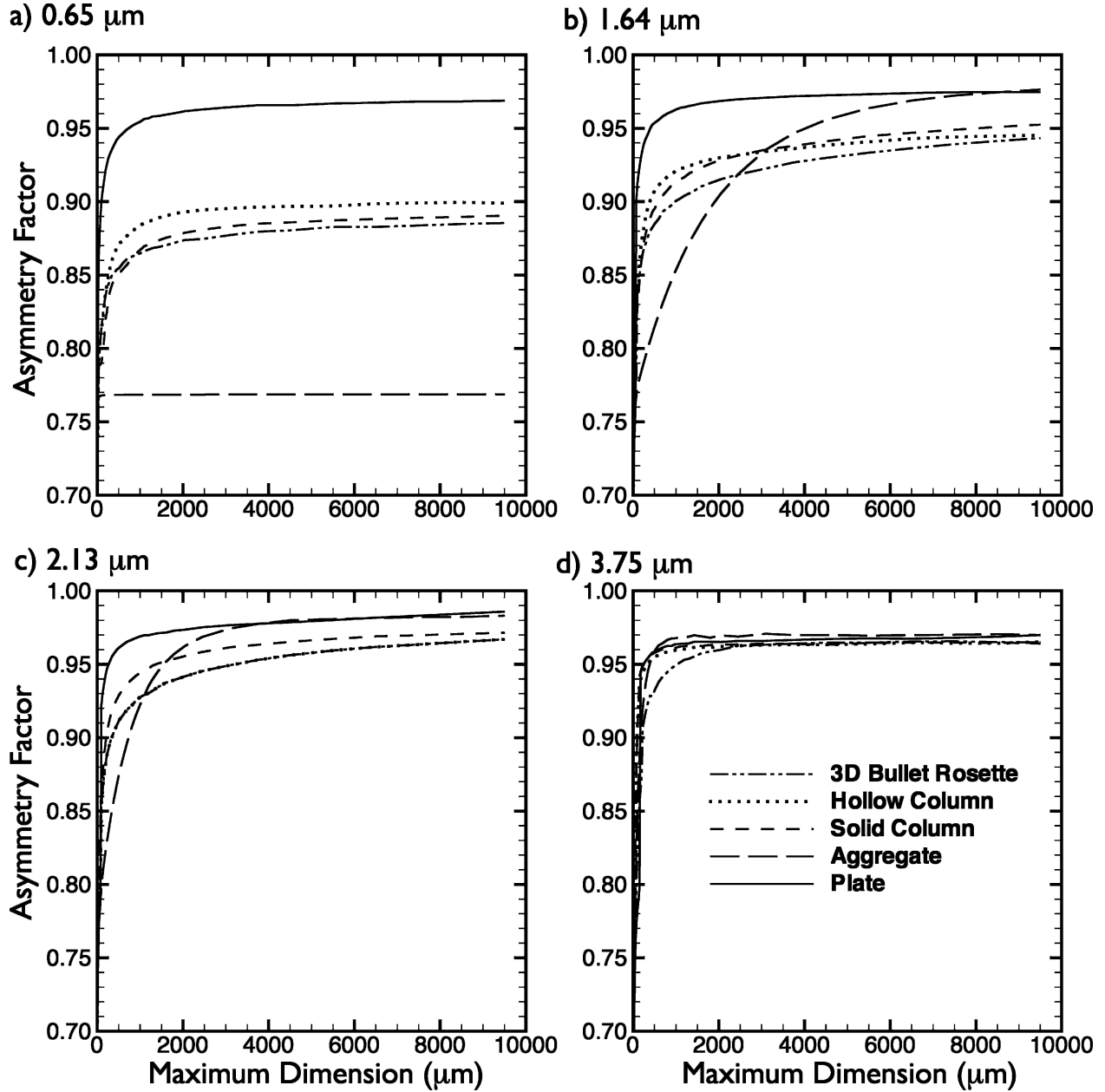
c) 2.13 μm

d) 3.75 μm

FIG. 2. Asymmetry factor at specific wavelengths of (a) 0.65, (b) 1.64, (c) 2.13, and (d) 3.75 μm as a function of $D_{\max}$ for five ice particle habits (3D bullet rosette, hollow column, solid column, aggregate, and hexagonal plate).

$$\overline{\sigma}_{\mathrm{ext}} = \frac{\int_{\lambda_1}^{\lambda_2} \int_{D_{\min}}^{D_{\max}} \left[\sum_{h=1}^{M} \sigma_{\mathrm{ext},h}(D, \lambda) f_h(D) \right] \times n(D) F_s(\lambda) S(\lambda) \, dD \, d\lambda}{\int_{\lambda_1}^{\lambda_2} \int_{D_{\min}}^{D_{\max}} \left[\sum_{h=1}^{M} f_h(D) \right] n(D) F_s(\lambda) S(\lambda) \, dD \, d\lambda}.$$

(5)

The single-scattering albedo $\overline{\omega}$ is determined by the ratio of the mean scattering and extinction cross sections:

$$\overline{\omega} = \frac{\overline{\sigma}_{\mathrm{sca}}}{\overline{\sigma}_{\mathrm{ext}}}.$$

(6)

Also of interest is the band-averaged scattering phase function
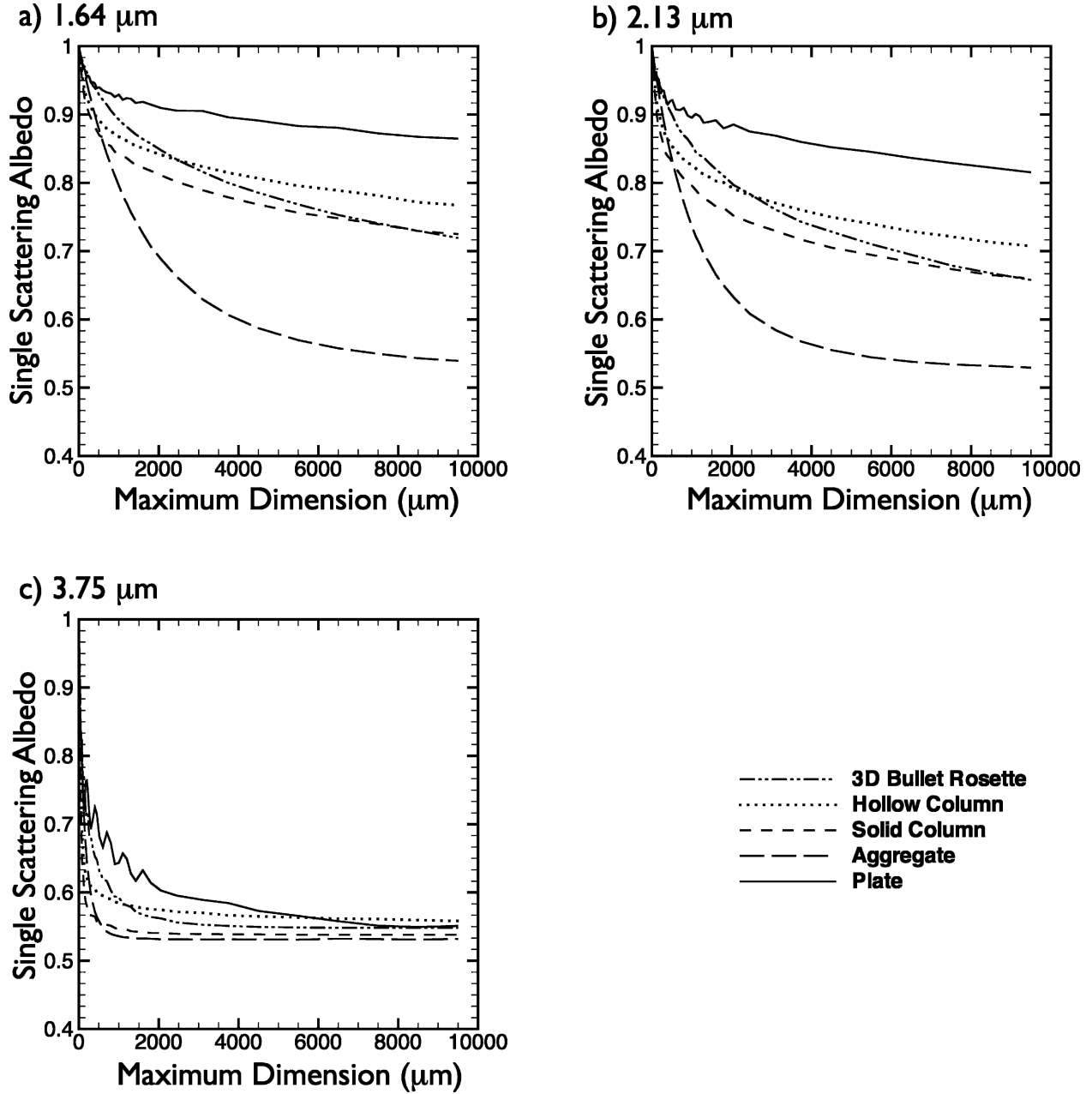
a) 1.64 μm

b) 2.13 μm

c) 3.75 μm

FIG. 3. Single-scattering albedo at specific wavelengths of (a) 1.64, (b) 2.13, and (c) 3.75 μm as a function of D_{max} for five ice particle habits (3D bullet rosette, hollow column, solid column, aggregate, and hexagonal plate).

$$\overline{P}(\Theta) = \frac{\int_{\lambda_1}^{\lambda_2} \int_{D_{min}}^{D_{max}} \left[\sum_{h=1}^{M} P_h(\Theta, D, \lambda)\sigma_{sca,h}(D, \lambda)f_h(D) \right] \times n(D)F_s(\lambda)S(\lambda)\, dD\, d\lambda}{\int_{\lambda_1}^{\lambda_2} \int_{D_{min}}^{D_{max}} \left[\sum_{h=1}^{M} \sigma_{sca,h}(D, \lambda)f_h(D) \right] \times n(D)F_s(\lambda)S(\lambda)\, dD\, d\lambda}.$$

(7)

TABLE 1. Spectral and radiometric characteristics of MODIS spectral bands for which results are shown in this study.

MODIS band	Wavelength range (μm)	Principal absorbing components
1	0.62–0.67	H_2O, O_3
6	1.628–1.652	H_2O, CO_2, CH_4
7	2.105–2.155	H_2O, CO_2, CH_4, N_2O
20	3.66–3.84	H_2O, CO_2, CH_4

Note that the phase function is weighted by the scattering cross section in the integrand. The band-averaged asymmetry factor $\overline{g}$ and fraction of δ transmission energy $\overline{f}_\delta$ are also weighted by the scattering cross section:

$$
\overline{g} = \frac{\displaystyle\int_{\lambda_1}^{\lambda_2}\int_{D_{\min}}^{D_{\max}}\left[\sum_{h=1}^{M} g_h(D,\lambda)\sigma_{\mathrm{sca},h}(D,\lambda)f_h(D)\right]}{\displaystyle\int_{\lambda_1}^{\lambda_2}\int_{D_{\min}}^{D_{\max}}\left[\sum_{h=1}^{M} \sigma_{\mathrm{sca},h}(D,\lambda)f_h(D)\right]} \quad \text{and}
$$

$$
\times\, n(D)F_s(\lambda)S(\lambda)\,dD\,d\lambda
$$
$$
\times\, n(D)F_s(\lambda)S(\lambda)\,dD\,d\lambda
$$

(8)

$$
\overline{f}_\delta = \frac{\displaystyle\int_{\lambda_1}^{\lambda_2}\int_{D_{\min}}^{D_{\max}}\left[\sum_{h=1}^{M} f_{\delta,h}(D,\lambda)\sigma_{\mathrm{sca},h}(D,\lambda)f_h(D)\right]}{\displaystyle\int_{\lambda_1}^{\lambda_2}\int_{D_{\min}}^{D_{\max}}\left[\sum_{h=1}^{M} \sigma_{\mathrm{sca},h}(D,\lambda)f_h(D)\right]} .
$$

$$
\times\, n(D)F_s(\lambda)S(\lambda)\,dD\,d\lambda
$$
$$
\times\, n(D)F_s(\lambda)S(\lambda)\,dD\,d\lambda
$$

(9)

The fraction of δ transmission energy for the IR bands is essentially zero because absorption dominates scattering within the crystal.

4. Results

In this section we present the bulk scattering properties obtained for 1117 particle size distributions. The cloud temperatures for these size distribution data range from $-25°$ to $-73°C$. Results are presented as a function of both the effective diameter and median mass diameter. The bulk scattering properties are presented for two habit distributions: one involving only solid hexagonal crystals and the other involving a mixture of particle habits, as described in Part I of this study. The MODIS V1 models are also included for comparison.

a. Band-averaged single-scattering albedo

Figure 4 shows the band-averaged single-scattering albedo $\overline{\omega}$ for MODIS bands 6 (1.64 μm), 7 (2.13 μm), and 20 (3.75 μm). The results obtained from hexagonal columns are in green, the results from a habit mixture are in black, and the 12 MODIS V1 models are in cyan. In general, the values of $\overline{\omega}$ decrease monotonically with increasing D_{eff} for each of these three MODIS bands.

Also, $\overline{\omega}$ decreases with increasing wavelength because of increasing absorption within the ice particles.

The highest $\overline{\omega}$ values correspond to the Cirrus Regional Study of Tropical Anvils and Cirrus Layers (CRYSTAL) Florida Area Cirrus Experiment (FACE) PSDs, which have the lowest D_{eff} values and the coldest cloud temperatures, as shown in Part I. It is interesting to note the bifurcation in the $\overline{\omega}$ values from hexagonal columns for all three MODIS bands. The values of $\overline{\omega}$ obtained from the habit mixture are higher overall for each of the three MODIS bands than those obtained from hexagonal columns only. This is primarily the result of including plates, hollow columns, and 3D bullet rosettes in the habit distribution. With the use of the habit mixture, the bifurcation is not as evident at higher values of D_{eff}.

Upon further investigation, the use of Tropical Rainfall Measuring Mission (TRMM) PSDs results in slightly higher values of $\overline{\omega}$ than those obtained from the FIRE-I, FIRE-II, Atmospheric Radiation Measurement Program (ARM), and CRYSTAL FACE campaigns. As noted in Part I, the TRMM PSDs have more small particles because the IWC values are higher, and, as shown in Fig. 3, the single-scattering albedo is highest for the smallest particles.

The MODIS V1 models have values of $\overline{\omega}$ that are generally consistent with those obtained from the habit mixture. With regard to D_{eff}, the range of values for MODIS V1 is much narrower than for the current results employing gamma size distributions. A given D_{eff} leads to similar values of $\overline{\omega}$ for both the MODIS V1 and gamma PSD results obtained for the habit mixture. One may also note that several of the MODIS V1 models have D_{eff} sizes that are smaller than any of those obtained from the use of the gamma PSDs. For these small D_{eff} values, the single-scattering albedo values are much higher than those of the gamma PSDs. However, the highest V1 $\overline{\omega}$ values tend to follow the monotonic relationship between D_{eff} and $\overline{\omega}$ noted previously. This result is further investigated and reported in section 4c.

b. Band-averaged asymmetry factor

We turn attention now to the asymmetry factor, which is the first moment of the scattering phase function. The asymmetry factor increases as the diffraction peak of the phase function sharpens and also increases with an increasing amount of δ transmission through ice particles, such as hexagonal plates, columns, and rosettes, with opposing but parallel faces. As shown in the section 2b, particles with $D_{\max} < 250$ μm have minimal contributions from δ transmission, as do aggregates of all sizes.

The band-averaged asymmetry factor $\overline{g}$ is shown in
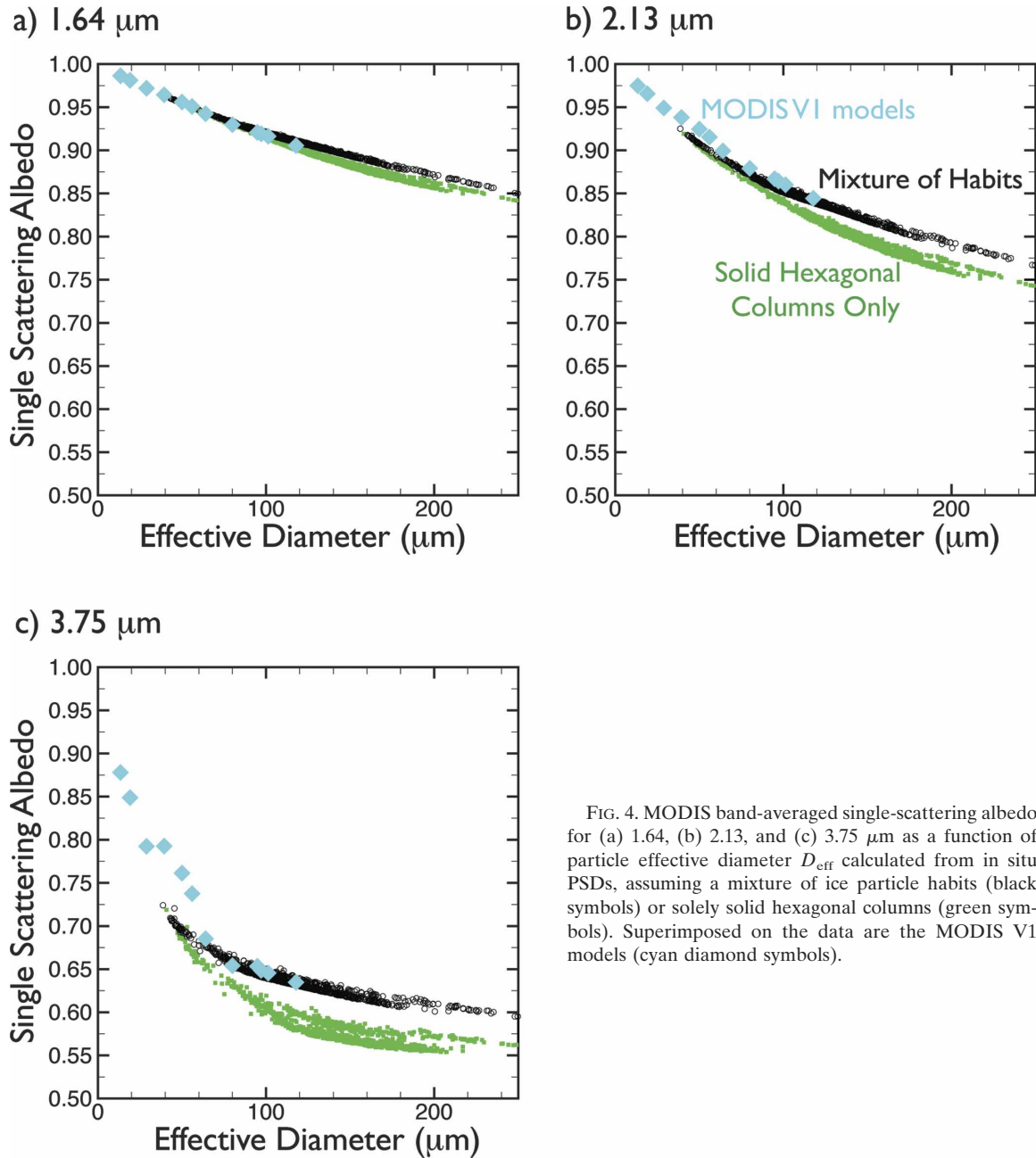
a) 1.64 μm

b) 2.13 μm

c) 3.75 μm

FIG. 4. MODIS band-averaged single-scattering albedo for (a) 1.64, (b) 2.13, and (c) 3.75 μm as a function of particle effective diameter D_{eff} calculated from in situ PSDs, assuming a mixture of ice particle habits (black symbols) or solely solid hexagonal columns (green symbols). Superimposed on the data are the MODIS V1 models (cyan diamond symbols).

Fig. 5 for calculations involving the PSDs using hexagonal columns only (green symbols) and a habit mixture (black symbols). The MODIS V1 models (cyan symbols) are provided for comparison. In general, the asymmetry factor tends to increase with D_{eff}. As D_{eff} increases past 100 μm, $\bar{g}$ reaches a limiting value. The values of $\bar{g}$ for TRMM tend to be lower than for the other field campaigns, leading to a bifurcation in $\bar{g}$ values. This behavior is attributed to the TRMM PSDs taking on the aspects of exponential size distributions rather than gamma size distributions. The exponential

size distribution tends to accentuate the number of very small particles, which tend to contribute very little to δ transmission. The TRMM PSDs also have more large particles, which, in our habit distribution, are composed primarily of bullet rosettes and aggregates. The modeled aggregates do not contribute to δ transmission.

Of real interest is the comparison of $\bar{g}$ between hexagonal columns and the ice habit mixture shown in Fig. 5. Because plates are used in the habit mixture, the contribution of δ transmission is expected to increase the value of $\bar{g}$ relative to that computed for columns

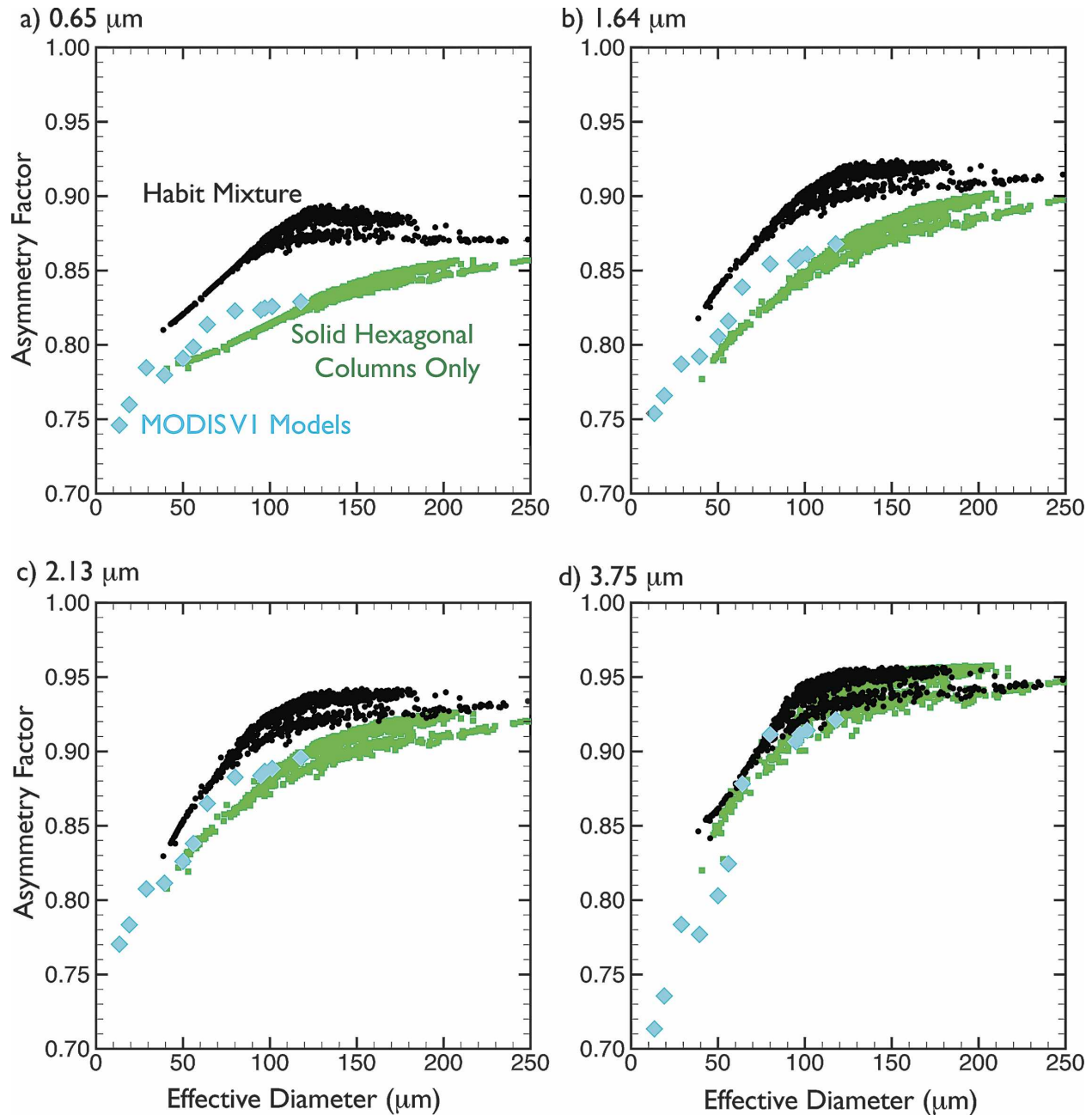FIG. 5. MODIS band-averaged asymmetry factor for (a) 0.65, (b) 1.64, (c) 2.13, and (d) 3.75 μm as a function of D_{eff} calculated from in situ PSDs, assuming a mixture of ice particle habits (black symbols) or solely solid hexagonal columns (green symbols). Superimposed on the data are the MODIS V1 models (cyan diamond symbols).

alone. The differences in MODIS bands 1, 6, and 7 are particularly striking. At 0.65 μm, the difference in $\bar{g}$ between columns and a habit mixture can be larger than 0.05, although the difference decreases as D_{eff} increases. For band 6 (1.64 μm), the asymmetry factor is higher by approximately 0.04 for D_{eff} sizes below 100 μm. The offset is evident also for band 7 but is minimal

for band 20 because of the influence of absorption within the ice particles.

Figure 5 additionally shows how the MODIS V1 $\bar{g}$ values compare with those computed from the various gamma PSDs using either of the habit distribution assumptions. At the shorter wavelengths (0.65 and 1.64 μm), the MODIS V1 model g values are considerably

lower in magnitude for a given D_{eff} than the values computed for a habit mixture but tend to be higher than those obtained assuming only hexagonal columns. The differences narrow as wavelength (and hence absorption) increases, especially at 3.75 μm. Part of the discrepancy might be explained by noting that the asymmetry factor tends to increase with particle size, especially at wavelengths with little absorption. Because more large particles are used in the PSDs than were used in the V1 models and some habits have significantly larger values of asymmetry factor than others, the band-averaged asymmetry factor for our chosen habit mixture is generally higher than that of the MODIS V1 models. The V1 model g values are higher in magnitude than those computed assuming only hexagonal columns. This result is expected because both plates and hollow columns are used in the mixture, and both tend to have higher asymmetry factors than solid columns.

Gerber et al. (2000) discuss the use of a cloud integrating nephelometer (CIN) to measure $\bar{g}$ at a visible wavelength. For an Arctic cloud involving glaciated cloud particles composed of large multibranched bullet rosettes, Gerber et al. determined $\bar{g}$ to be 0.737, which is substantially less than the mean value of $\bar{g}$ (0.835) that is found for water clouds. The largest sources of uncertainty are stated to be the amount of energy in the first 10° of the phase function, and the effect of δ transmission. To determine a CIN value for g, the CIN measurements must be scaled by the amount of energy in the forward peak. Gerber et al. estimate that the fraction of energy scattered in the forward 10° is 0.57 with an error limit of 2%. We note that the maximum dimension of the bullet rosettes listed in the Gerber et al. (2000) study did not extend to the sizes near 1 cm used in this study. Because larger particles are more forward scattering than are smaller particles, it may be that the fraction of energy in the forward peak could be substantially higher.

Garrett et al. (2003) present CIN analyses from low-latitude cirrus that are composed primarily of small crystals. Taken with other cirrus observations by Auriol et al. (2001) and Gerber et al. (2000), $\bar{g}$ ranges from 0.73 to 0.78. CIN measurements of arctic ice clouds reported in Garrett and Hobbs (2001) tend to fall in the same range. The CRYSTAL FACE PSDs have $\bar{g}$ in the same range as those from the extratropical measurements, but our model calculations have $\bar{g}$ increasing with effective diameter.

The results for a habit mixture demonstrate the potential influence of δ transmission on the asymmetry factor. Although the habit mixture we chose included plates, it could be argued that if pristine particles such as plates are not present then the asymmetry factor values could be much lower. Given this discussion, it would be interesting to reevaluate the CIN measurements given the extended set of ice particle scattering properties now available. At this point, we note the difference in $\bar{g}$ between our models and the CIN measurements, and we will address this issue in future research.

c. Sensitivity of $\bar{g}$ and $\bar{\omega}$ to small particles (small D_{eff})

In sections 4a and 4b, several of the MODIS V1 have smaller D_{eff} than those that are calculated based upon the set of 1117 gamma PSDs. The discrepancy between the V1 and gamma PSD sets of models can be explained through an examination of the respective sets of PSDs. In Part I of this study, their Fig. 1 showed a sampling of the gamma PSDs, as well as several of the V1 model PSDs. In these three V1 size distributions, there are roughly from one to two orders of magnitude more particles in the 20-μm size bin than in the 50-μm size bin, and particle density drops off quickly as size increases. Although more recent in situ ice cloud data benefit from improvements in measurement technology, the number of the smallest particles is still uncertain.

As a way to gain some sense of the sensitivity of small particles to D_{eff}, $\bar{g}$, and $\bar{\omega}$ calculations, we first note that the CRYSTAL FACE PSDs tend to be the most narrow. This is to be expected because they were derived from the coldest clouds in our dataset and have the lowest IWC values. Thus, the CRYSTAL FACE PSDs are adopted for the sensitivity study and are modified as follows: the particle number densities in the smallest size bins (<20 μm) are multiplied by 100 in the first set of calculations and by 1000 in the second set. By doing so, we will no longer be able to match closely with the in situ IWC values, but this is a simple experiment to gain some insight as to the sensitivity of the bulk scattering parameters to small particles.

Enhanced small-particle results for $\bar{\omega}$ and $\bar{g}$ are shown in Figs. 6 and 7. The results using the unmodified PSDs are shown in black or gray. The results obtained by multiplying the number of small particles by 100 (1000) are shown in green (red). The cyan squares represent the MODIS V1 models. The MODIS V1 models provide $\bar{\omega}$ values similar to those of the current calculations, at least at wavelengths of 1.64 and 2.13 μm, but there are some differences at 3.75 μm over a small range in D_{eff} between 40 and 60 μm. For $D_{eff} < 20$ μm, the MODIS V1 $\bar{\omega}$ values overlay those obtained from the modified CRYSTAL FACE PSDs.

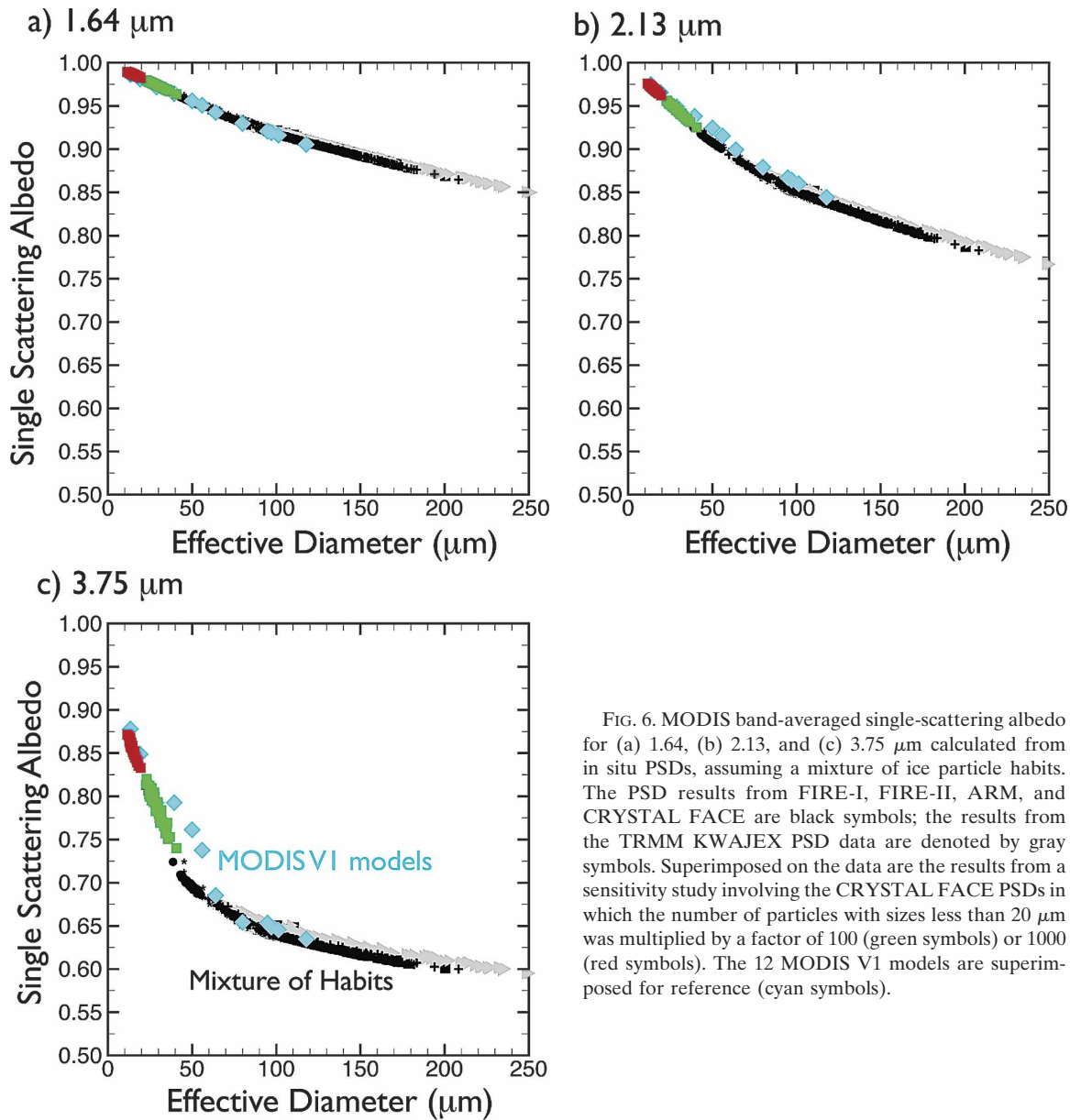The asymmetry factor seems to be sensitive to the ice-particle habit as shown in Figs. 5 and 7. The MODIS

a) 1.64 μm

b) 2.13 μm

c) 3.75 μm

MODIS V1 models

Mixture of Habits

FIG. 6. MODIS band-averaged single-scattering albedo for (a) 1.64, (b) 2.13, and (c) 3.75 μm calculated from in situ PSDs, assuming a mixture of ice particle habits. The PSD results from FIRE-I, FIRE-II, ARM, and CRYSTAL FACE are black symbols; the results from the TRMM KWAJEX PSD data are denoted by gray symbols. Superimposed on the data are the results from a sensitivity study involving the CRYSTAL FACE PSDs in which the number of particles with sizes less than 20 μm was multiplied by a factor of 100 (green symbols) or 1000 (red symbols). The 12 MODIS V1 models are superimposed for reference (cyan symbols).

V1 models' $\bar{g}$ values do not exactly match those from the current set of PSDs, but that is probably due to the use of a different habit distribution. In these calculations, the comparison seems to hint at larger differences for $D_{eff} > 80$ μm. This is expected because the current results are based on integration of particle size over 45 size bins, whereas the V1 models employed only 5 size bins.

d. Scattering phase functions

A discussion of the scattering phase functions follows in this section. To facilitate this discussion, the full set of phase functions for each MODIS band [derived following Eq. (7)] is filtered and averaged as follows. The goal is to develop phase functions for a defined set of D_{eff}, which in this case is $D_{eff} = 10$–180 μm in increments of 10 μm, for a total of 18 discrete D_{eff} values. We note that the only way to obtain phase functions, or any of the bulk scattering parameters for that matter, for D_{eff} at sizes of less than 30 μm is to modify the PSDs by increasing the number of small particles as discussed in the previous section. The set of phase functions is augmented by the two sets of properties resulting from the modified CRYSTAL FACE PSDs (i.e., one set in which the number of small particles is multiplied by
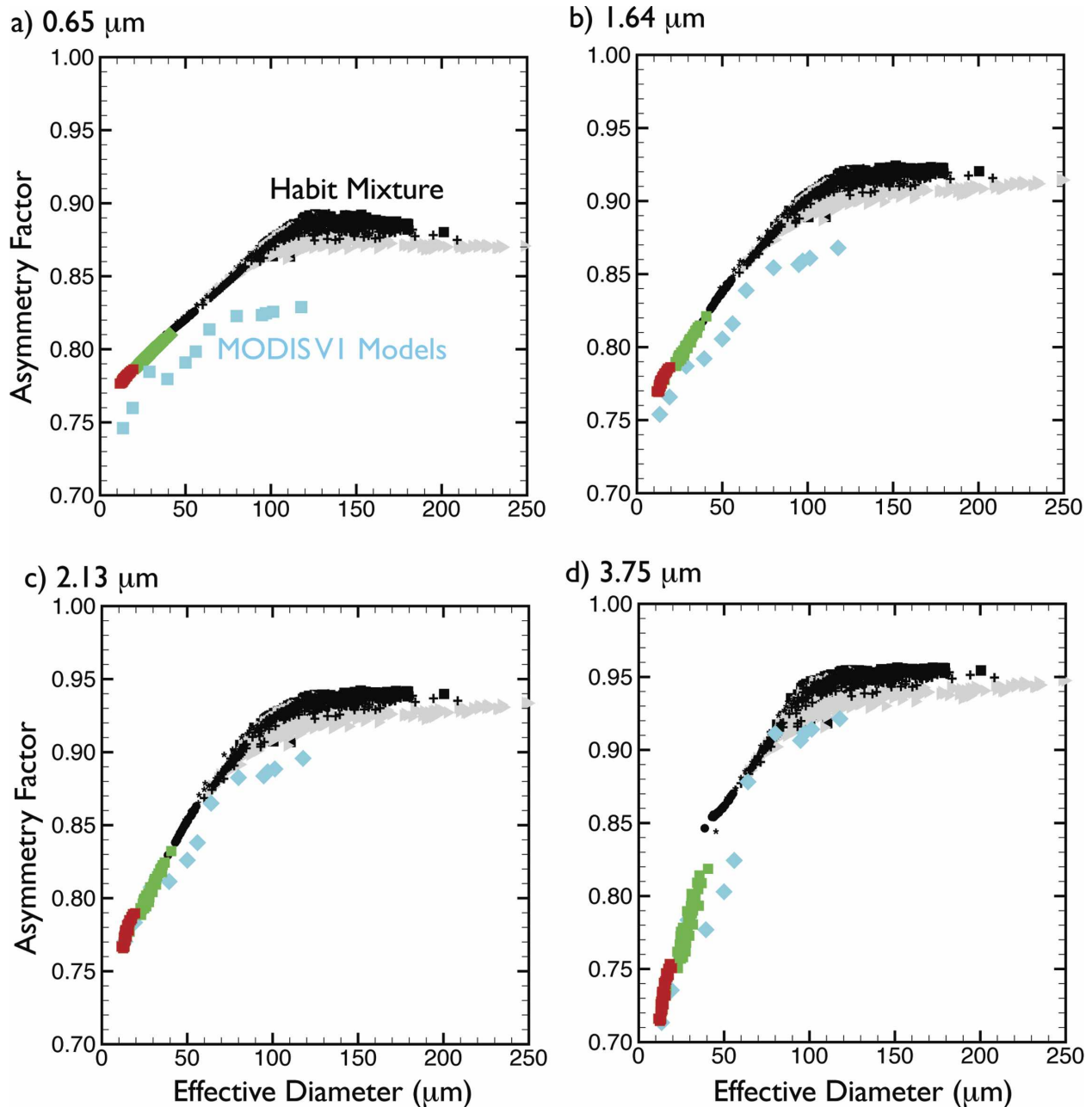
a) 0.65 μm

b) 1.64 μm

c) 2.13 μm

d) 3.75 μm

FIG. 7. Same as for Fig. 6, but for MODIS band-averaged asymmetry factor for (a) 0.65, (b) 1.64, (c) 2.13, and (d) 3.75 μm.

100, and the other set in which the number is multiplied by 1000).

The PSDs that fall within a narrow region around the target D_{eff} values are averaged; the width of the region is chosen such that between 10 and 20 individual PSDs can be averaged for each D_{eff}. For each D_{eff} value, a mean and standard deviation can be calculated for the phase function. A benefit to this approach is that the mean and standard deviation values, for not only the

phase functions but the other scattering properties as well, can be used to estimate retrieval errors.

Results for D_{eff} values of 20, 60, and 100 μm are shown in Fig. 8 for the MODIS 1.64-μm band. The left-hand column shows the phase function over the full 180° range in scattering angle Θ, and the right-hand column shows the phase function over the forward peak in the scattering angle. At 20 μm, the largest variances occur at very small Θ of less than 2°. At $D_{eff} = 60$ and
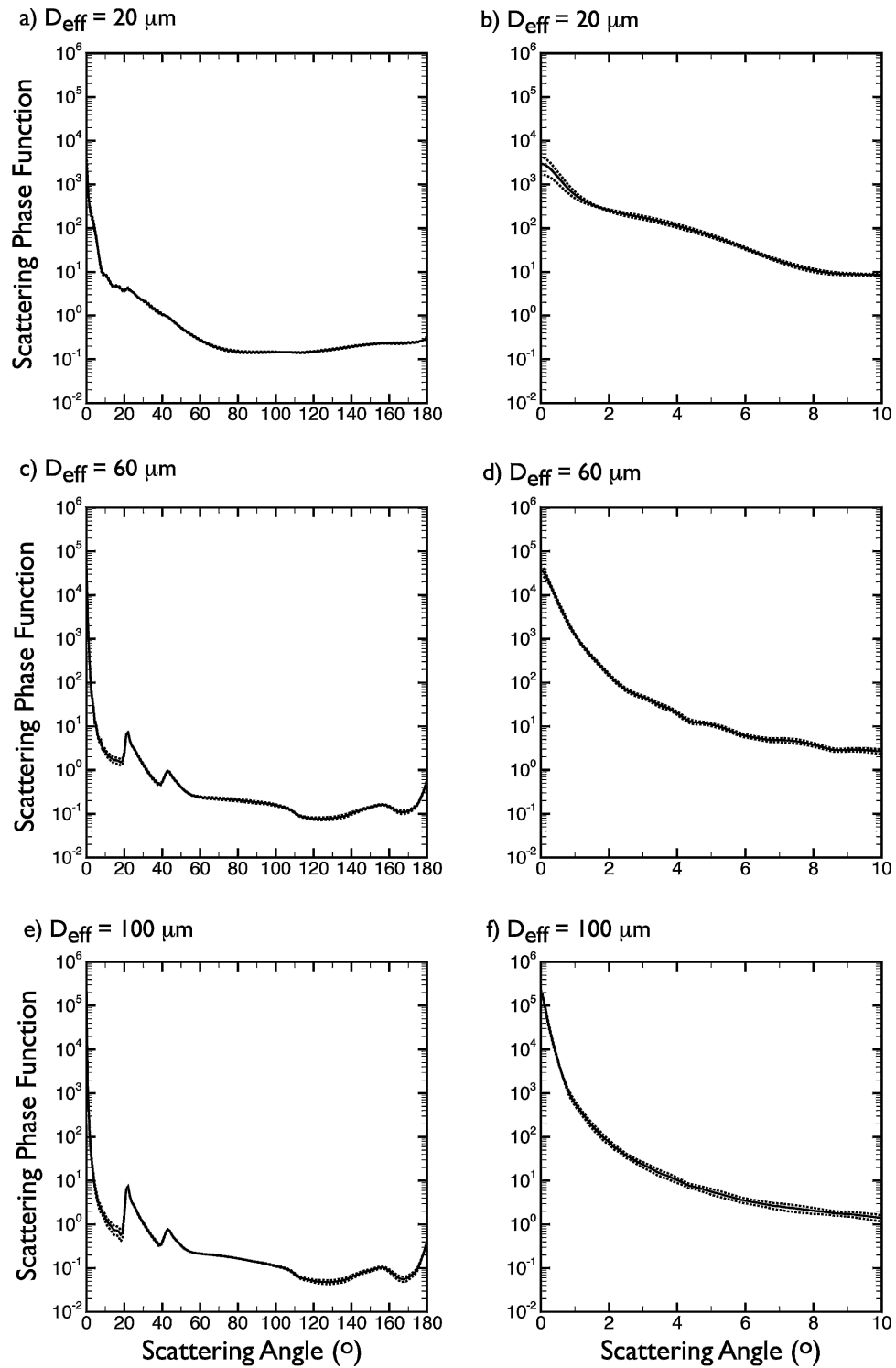
a) $D_{eff} = 20 \ \mu m$

b) $D_{eff} = 20 \ \mu m$

c) $D_{eff} = 60 \ \mu m$

d) $D_{eff} = 60 \ \mu m$

e) $D_{eff} = 100 \ \mu m$

f) $D_{eff} = 100 \ \mu m$

FIG. 8. For MODIS band 6 (1.64 μm), the scattering phase function mean (solid line) and standard deviation (dotted line) for D_{eff} values of (top) 20, (middle) 60, and (bottom) 100 μm are shown for (a), (c), (e) the full phase function and (b), (d), (f) the forward peak in the phase function.
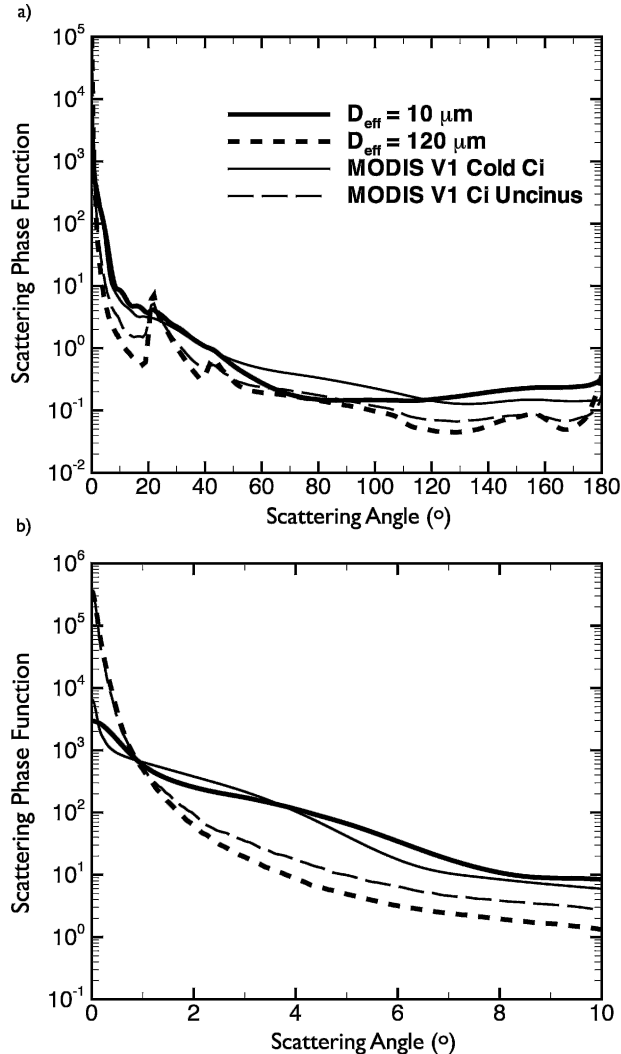
a)

b)

FIG. 9. For MODIS band 6 (1.64 μm), a comparison of the two MODIS V1 models (cold Ci, D_{eff} = 13.4 μm; Ci uncinus, D_{eff} = 117.8 μm) with two new models at D_{eff} = 10 and 120 μm for (a) the full scattering phase function and (b) the first 10° of the scattering phase function.

100 μm, the largest variances occur near the minima at Θ = 20°, 130°, and 170°.

A comparison with two of the MODIS V1 models is shown in Fig. 9, again for the MODIS 1.64-μm band. The MODIS V1 cold cirrus (cold Ci) model and the cirrus uncinus (Ci uncinus) models (Baum et al. 2000) are chosen because they represent the extrema of the V1 models, having the smallest and largest D_{eff} values, respectively, of 13.4 and 117.8 μm. Note that the D_{eff} values provided in Baum et al. (2000) are lower than the values provided here; this difference is a result of a slightly different definition of effective diameter in the earlier study that did not include multiplication by a constant of 3/2. The averaged phase functions derived

at D_{eff} of 10 and 120 μm are provided for comparison with the cold Ci and Ci uncinus V1 models. The upper panel of Fig. 9 shows the full phase function, and the lower panel shows only the forward peak.

A comparison of the two small-particle models (cold Ci and D_{eff} = 10 μm) shows some interesting differences. The value of the phase function is higher for the V1 cold Ci model than for the D_{eff} = 10 μm model, both in the forward-scattering direction (Θ < 3°) and at side-scattering angles between 50° and 110°. However, for 4° < Θ < 30°, and at Θ > 120°, the reverse is true. The primary difference between the two models is in the use of droxtals. Droxtals have some of the tendencies of spherical particles in that the side scattering is reduced in comparison with hexagonal columns and backscattering is enhanced.

The two large-particle models (Ci uncinus and D_{eff} = 100 μm) match more closely than do the small-particle models. However, there are some regions where differences exist near the minima at Θ = 20°, 40°, and 170° and for 110° < Θ < 140°. The two models are very similar in the magnitudes of the phase function in both the forward and backward peaks.

5. Summary

This study examines the development of bulk single-scattering properties, including single-scattering albedo, asymmetry factor, and phase function, for a set of 1117 particle size distributions. The primary focus is to develop band-averaged models that are appropriate for use by the MODIS imager on the EOS *Terra* and *Aqua* platforms, but the method can be applied easily to other imagers such as the Advanced Very High Resolution Radiometer or the Along-Track Scanning Radiometer. The primary MODIS bands discussed in this study are located at wavelengths of 1.64, 2.13, and 3.75 μm. These bands are chosen because of their use in inferring ice cloud optical thickness and effective particle size. The primary benefit derived from application of our method is that the microphysical attributes of each model, specifically median mass diameter and ice water content, are consistent with those obtained from the in situ measurements as discussed in Part I. This aspect should help to facilitate comparisons of satellite-derived quantities with those obtained from ground-based or aircraft-based measurements.

The PSDs are derived from analysis of FIRE-I, FIRE-II, ARM intensive operating periods, TRMM KWAJEX, and CRYSTAL FACE data. However, only the TRMM KWAJEX data are obtained from tropical cirrus anvils. The PSDs for the TRMM data tend to follow exponential distributions rather than gamma dis-

tributions. For any given ice-particle habit mixture, the bulk scattering properties of asymmetry factor and single-scattering albedo tend to fall into two groups, with one group containing the FIRE, ARM, and CRYSTAL FACE data, and the other group containing the TRMM data. We note that the CRYSTAL FACE data are from an extremely cold, optically thin cirrus cloud near the tropopause rather than from an anvil associated with deep convection. The data indicate that there are substantial differences between ice clouds formed in areas of deep convection and those that exist in areas of much lower updraft velocities.

Results obtained from a particle-size-dependent mixture of ice crystal habits are compared with those obtained by assuming only solid hexagonal columns. The single-scattering albedo is lower for hexagonal columns than for a habit mixture for the 1.64-, 2.13-, and 3.75-μm bands, with the differences increasing with wavelength. In contrast, the asymmetry factors obtained from the habit mixture and only the solid hexagonal columns are most different at 0.65 μm, with the differences becoming lower as wavelength increases. At 3.75 μm, the asymmetry factor results from the two habit assumptions are almost indistinguishable. The asymmetry factor is found to be sensitive to the largest particles and particle habits assumed in the size distributions.

Results for asymmetry factor and single-scattering albedo are also compared with the MODIS V1 models. The V1 models have values for effective diameter that are much smaller than those obtained from the 1117 PSDs. Further examination into this discrepancy showed that the number of small particles in the smallest size bin of the V1 models was from two to three orders of magnitude higher than for the gamma distributions. Because the number of small particles is unknown because of the difficulty in measuring them accurately, two additional sets of PSDs were obtained by modifying the CRYSTAL FACE PSD set in the following fashion: one set was derived by multiplying the number of small particles in the gamma distribution (i.e., those particles having a maximum dimension of less than 20 μm) by a factor of 100, and the other set was derived by multiplying the small crystals by a factor of 1000. The CRYSTAL FACE PSD set was chosen because it was sampled from the coldest cloud in the dataset and also had the lowest IWC values. Based on the "modified" CRYSTAL FACE PSDs, the effective diameter was extended from a minimum of 30 to 10 μm. Although arbitrary, this provides some insight as to the sensitivity of bulk scattering properties to the number of small particles.

Future research will be performed to assess further the difference between bulk scattering models obtained from ice clouds in convective versus nonconvective regions. Also, we hope to revisit the small-particle issue once more accurate measurements are available.

REFERENCES

Auriol, F., J.-F. Gayet, G. Febvre, O. Jourdan, O. L. Labomote, and G. Brogniez, 2001: In situ observation of cirrus scattering phase functions with 22° and 46° halos: Cloud field study on 19 February 1998. *J. Atmos. Sci.,* **58,** 3376–3390.

Barnes, W. L., T. S. Pagano, and V. V. Salomonson, 1998: Prelaunch characteristics of the Moderate Resolution Imaging Spectroradiometer (MODIS) on EOS-AM1. *IEEE Trans. Geosci. Remote Sens.,* **36,** 1088–1100.

Baum, B. A., D. P. Kratz, P. Yang, S. Ou, Y. Hu, P. F. Soulen, and S.-C. Tsay, 2000: Remote sensing of cloud properties using MODIS Airborne Simulator imagery during SUCCESS. I. Data and models. *J. Geophys. Res.,* **105,** 11 767–11 780.

——, A. J. Heymsfield, P. Yang, and S. T. Bedka, 2005: Bulk scattering properties for the remote sensing of ice clouds. Part I: Microphysical data and models. *J. Appl. Meteor.*, **44,** 1885–1895.

Garrett, T. J., and P. V. Hobbs, 2001: Shortwave, single scattering properties of arctic ice clouds. *J. Geophys. Res.,* **106,** 15 155–15 172.

——, H. Gerber, D. G. Baumgardner, C. H. Twohy, and E. M. Weinstock, 2003: Small, highly reflective ice crystals in low-latitude cirrus. *J. Geophys. Lett.,* **30,** 2132, doi:10.1029/2003GL018153.

Gerber, H., Y. Takano, T. J. Garrett, and P. V. Hobbs, 2000: Nephelometer measurements of the asymmetry parameter, volume extinction coefficient, and backscatter ratio in Arctic clouds. *J. Atmos. Sci.,* **57,** 3021–3034.

Heymsfield, A. J., 1975: Cirrus uncinus generating cells and the evolution of cirroform clouds. Part I. Aircraft observations of the growth of the ice phase. *J. Atmos. Sci.,* **32,** 799–808.

——, and C. M. R. Platt, 1984: A parameterization of the particle size spectrum of ice clouds in terms of the ambient temperature and the ice water content. *J. Atmos. Sci.,* **41,** 846–855.

King, M. D., Y. J. Kaufman, W. P. Menzel, and D. Tanré, 1992: Remote sensing of cloud, aerosol, and water vapor properties from the Moderate Resolution Imaging Spectrometer (MODIS). *IEEE Trans. Geosci. Remote Sens.,* **30,** 2–27.

——, S. Platnick, P. Yang, G. T. Arnold, M. A. Gray, J. C. Riédi, S. A. Ackerman, and K. N. Liou, 2004: Remote sensing of liquid water and ice cloud optical thickness and effective radius in the Arctic: Application of airborne multispectral MAS data. *J. Atmos. Oceanic Technol.,* **21,** 857–875.

Kurucz, R. L., I. Furenlid, J. Brault, and L. Testerman, 1984: Solar flux atlas from 296 to 1300 nm. *National Solar Observatory Atlas No. 1*, National Solar Observatory, 239.

Nasiri, S. L., B. A. Baum, A. J. Heymsfield, P. Yang, M. Poellot,

D. P. Kratz, and Y. Hu, 2002: Development of midlatitude cirrus models for MODIS using FIRE-I, FIRE-II, and ARM in situ data. *J. Appl. Meteor.,* **41,** 197–217.

Neckel, H., and D. Labs, 1984: The solar radiation between 3300 and 12500 angstroms. *Sol. Phys.,* **90,** 205–258.

Platnick, S., M. D. King, S. A. Ackerman, W. P. Menzel, B. A. Baum, J. C. Riédi, and R. A. Frey, 2003: The MODIS cloud products: Algorithms and examples from *Terra. IEEE Trans. Geosci. Remote Sens.,* **41,** 459–473.

Takano, Y., and K. N. Liou, 1989: Radiative transfer in cirrus clouds. Part I: Single-scattering and optical properties of oriented hexagonal ice crystals. *J. Atmos. Sci.,* **46,** 3–19.

Yang, P., and K. N. Liou, 1996a: Finite-difference time domain method for light scattering by small ice crystals in three-dimensional space. *J. Opt. Soc. Amer. Assoc.,* **13,** 2072–2085.

——, and ——, 1996b: Geometric-optics-integral-equation method for light scattering by nonspherical ice crystals. *Appl. Opt.,* **35,** 6568–6584.

——, and ——, 1998: Single scattering properties of complex ice crystals in terrestrial atmosphere. *Contrib. Atmos. Phys.,* **71,** 223–248.

——, B. A. Baum, A. J. Heymsfield, Y. X. Hu, H.-L. Huang, S.-C. Tsay, and S. Ackerman, 2003: Single scattering properties of droxtals. *J. Quant. Spectrosc. Radiat. Transfer,* **79-80,** 1159–1169.

Zhang, Z., P. Yang, G. W. Kattawar, S.-C. Tsay, B. A. Baum, Y. X. Hu, A. J. Heymsfield, and J. Reichardt, 2004: Geometric optics solution for the scattering properties of droxtal ice crystals. *Appl. Opt.,* **43,** 2490–2499.